

Optimization of the Energy-Comfort Trade-Off of HVAC Systems in Electric City Buses Based on a Steady-State Model

Fabio Widmer, Stijn van Dooren, Christopher H. Onder

Institute for Dynamic Systems and Control, ETH Zürich, 8092 Zürich, Switzerland

Abstract

The electrification of public transport vehicles offers the potential to relieve city centers of pollutant and noise emissions. Furthermore, electric buses have lower life-cycle greenhouse gas (GHG) emissions than diesel buses, particularly when operated with sustainably produced electricity. However, the heating, ventilation, and air-conditioning (HVAC) system can consume a significant amount of energy, thus limiting the achievable driving range. In this paper, we address the HVAC system in an electric city bus by analyzing the trade-off between the energy consumption and the thermal comfort of the passengers. We do this by developing a dynamic thermal model for the bus, which we simplify by considering it to be in steady state. We introduce a method that is able to quickly optimize the steady-state HVAC system inputs for a large number of samples representative of a year-round operation. A comparison between the results from the steady-state optimization approach and a dynamic simulation reveals small deviations in both the HVAC system power demand and achieved thermal comfort. Thus, the approximation of the system performance with a steady-state model is justified. We present two case studies to demonstrate the practical relevance of the approach. First, we show how the method can be used to compare different HVAC system designs based on a year-round performance evaluation. Second, we show how the method can be used to extract setpoints for online controllers that achieve close-to-optimal performance without any predictive information. In conclusion, this study shows that a steady-state analysis of the HVAC systems of an electric city bus is a valuable approach to evaluate and optimize its performance.

Keywords: HVAC, public transport, thermal comfort, electric mobility, optimization, city bus

1. Introduction

1.1. Motivation

In the face of global warming, an increasing number of countries are committing themselves to net-zero emission targets [1]. Transportation is a substantial contributor to emissions, accounting for around 20% of global CO₂ emissions, with nearly half of that originating from road-based passenger transport [2].

Both public transport and vehicle electrification can help to decrease the carbon footprint of passenger transport. In fact, electric buses achieve approximately 65% less greenhouse gas (GHG) emissions than diesel buses and 75% less than private gasoline vehicles per passenger kilometer during operation [3]. Even if lifetime GHG emissions are considered and even if a very high grid carbon intensity is assumed, electric buses are preferable over diesel-powered buses [4]. Beyond global emissions reduction, electric propulsion in public transport can mitigate local environmental impacts in city centers, alleviating issues such as noise and pollutant emissions. Furthermore, public transportation utilizes significantly less space per passenger kilometer compared to private vehicles [5], which is an important consideration in densely populated urban areas. For these reasons, a widespread adoption of battery electric vehicles (BEVs) in public transport is desirable.

While BEVs offer the aforementioned benefits, they also pose technical challenges. One prominent issue is the high energy demand of the heating, ventilation, and air-conditioning (HVAC) system during seasons that require heating, as BEVs do not have an abundant heat source like diesel-powered vehicles. Furthermore, public transport vehicles, in particular city buses, are typically poorly insulated and are subject to frequent openings of large doors. For instance, the overall energy consumption of an electric city bus was shown to double during winter conditions due to the HVAC system operation [6]. This places heavy constraints on the achievable driving range in battery-powered applications.

Achieving a reduction in HVAC energy consumption typically conflicts with thermal comfort requirements. Thus, most research on HVAC systems in public transportation vehicles focuses on enhancing the trade-off between these competing goals. Improvements of this trade-off can be achieved along two primary paths, which can be treated independently or in conjunction: improving the *design* or enhancing the *control* of HVAC systems. In the subsequent review section, we analyze and categorize existing literature on both of these topics.

1.2. Literature Review

For the design and control of HVAC systems, distinctions emerge when comparing public transportation applications to those of other domains. *Passenger vehicles* are usually operated

Email address: fawidmer@idsc.mavt.ethz.ch (Fabio Widmer)

for short periods of time. Thus, most research focuses on transient scenarios like heat-up or cool-down [7, 8]. This requires dynamic models, for which frameworks [9] or purpose-built simulation tools [10] have been suggested. In contrast, public transportation vehicles are typically operated for extended periods of time and thus, the transient phases of heat-up and cool-down are much less relevant. Compared to vehicular applications, thermal capacity and insulation values of *buildings* are significantly higher, leading to thermal timescales on the order of hours. Thus, models are almost uniquely dynamic [11, 12] and predictive control is commonly used to plan the corresponding thermal trajectories in accordance with weather forecast [13, 14]. On the other hand, transit buses exhibit a thermal timescale on the order of ten minutes [15, 16]. This is significantly faster than the changing ambient conditions, such as the ambient temperature. In summary, the long duration of driving missions and the comparably short timescales of the thermal systems in transit buses potentially allow for the application of steady-state models.

However, most research that deals with HVAC *control optimization* in public transportation applications is based on dynamic models. For instance, dynamic models are employed to assess heuristic controller designs [17], to evaluate objective functions during genetic algorithm (GA)-based optimization of control parameters [18], to implement multi-level model predictive control (MPC) approaches [19, 20], or as a training basis for long short-term memory (LSTM) neural networks that are used in a neural network MPC algorithm [21]. In contrast, the utilization of steady-state models for controller design and optimization is rare. Instances include the use of a static black-box model, derived from real-life measurements, to assess temperature setpoint changes [22], and the analysis of steady-state simulation results of a passenger car to generate controller setpoints [23].

In the area of *design optimization*, dynamic models are also the most common option. Several researchers propose simulation methods to estimate the energy consumption of HVAC systems using dynamic models [15, 24, 25, 26, 27]. While these publications do not directly show comparisons between system designs, the models are typically motivated by such objectives. Some researchers directly compare the performance of different HVAC systems based on dynamic models in buses [28, 29] or trains [30]. With a few exceptions, steady-state models are rarely used. For instance, models from first principles are evaluated in steady-state to suggest an extension of the worldwide-harmonized light vehicles test procedure (WLTP) to include HVAC loads [31] or to evaluate the effectiveness of system components like heat pumps (HPs) and radiant heaters (RHs) [32]. Alternatively, based on measurement data, data-driven steady-state models can be developed for the HVAC system consumption within a larger energy consumption estimation framework [33], or even for the entire vehicle consumption calculation, which enables evaluating various design changes [34].

Due to their inherently high computational demands, dynamic models, whether used for control or design purposes, are inadequate to analyze year-round operation. For this reason, usually only simplified problems involving a single scenario are

considered [20, 23, 29]. Many researchers attempt to approximate the year-round operation by considering a small sample of up to ten scenarios, e.g., [8, 17, 18, 19, 24, 26, 27]. These scenarios are typically based on heuristic approaches or expert knowledge, e.g., by selecting representative days for each season [17] or for nine different weather classes [24] or “typical” days for each month [27]. An alternate approach is to base the scenario selection on machine learning tools. For instance, some researchers suggest using clustering algorithms to find representative scenarios [35, 36]. Only a limited number of researchers use dynamic models to fully consider year-round influences. This can be achieved by simulating every day over an entire year [30] or by using a reference year and categorizing days based on their average temperatures to limit the number of simulations [28]. An alternate approach is to avoid frequent evaluations of a computationally expensive model by creating a surrogate energy consumption model whose parameters are tuned with Monte Carlo simulations [25]. Similarly, a surrogate model-based optimization of the charging infrastructure under consideration of all loads, including HVAC system consumption, is suggested in [37], allowing the optimization to be based on a large number of driving missions.

Conversely, the comparatively low computational demand of steady-state models facilitates the evaluation of the annual performance. To this end, various methods can be used, such as Monte Carlo simulations [22], weighted averages with the frequency of different temperature ranges [31], or computing hourly averages for realistic operating hours [32, 34].

1.3. Research Statement

In previous research, some researchers have suggested the application of steady-state models for the HVAC system of public transportation vehicles. Utilizing a steady-state thermal model rather than a dynamic one significantly reduces the computational time required for simulations or for solving optimization problems. This efficiency enhancement facilitates the evaluation of year-round performance. However, to the best of our knowledge, none of the published research based on steady-state models provides quantitative comparisons or evidence why such an approach is appropriate. In this paper, we fill this gap by conducting a quantitative comparison between steady-state optimization and dynamic simulation results. Furthermore, we explore the possibility of leveraging steady-state models for both system design comparisons and control improvements.

1.4. Paper Structure

This paper is structured as follows. In [Section 2](#), we introduce the thermal model of a city bus cabin and its HVAC system. We explain how we quantify thermal comfort, introduce the disturbances and their data sources, and introduce the steady-state approximation of the model. In [Section 3](#), we formulate the optimization problem based on the steady-state model and present a method to solve it. In [Section 4](#), we present and discuss the results. Finally, in [Section 5](#), we draw conclusions and make suggestions for further research.

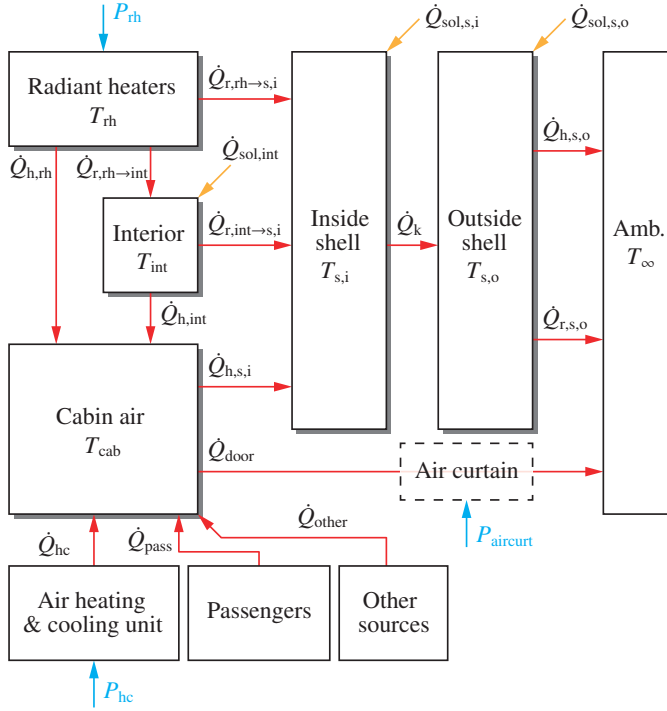


Figure 1: Model component overview. Thermal reservoirs are represented as shaded blocks. Red arrows denote heat flows, yellow arrows denote solar heat gain, and blue arrows denote electric power flows. Time dependencies are omitted for clarity.

2. System Modeling

In this section, we first introduce a dynamic thermal model of the passenger cabin and the HVAC system of an electric city bus. We then explain how we quantify thermal comfort and introduce the data sources used for our case studies. Finally, we introduce a steady-state approximation of the model, which forms the basis for optimizing the HVAC operation as described in Section 3. All model constants are listed in Appendix A.

2.1. Dynamic Thermal Model

Figure 1 provides an overview of the thermal model of the passenger cabin and the HVAC system of an electric city bus. It depicts all model components along with all the heat and power flows.

The bus cabin and its shell are modeled using five thermal reservoirs, which are characterized by their respective temperature. The cabin air temperature $T_{cab}(t)$ represents the thermal environment for the passengers. For the sake of simplicity, we model the entire cabin with one uniform temperature and do not separately treat the driver compartment. The bus interior, which includes the seats and hand rails, is modeled with one lumped thermal capacity with temperature $T_{int}(t)$. As the interior is in convective heat exchange with the surrounding cabin air, it has a smoothing effect on the cabin air temperature during transients, reducing the impact of sudden changes in heat flows, such as those caused by door openings. We model the bus shell with two separate components, namely an *inside* shell and an *outside* shell with temperatures $T_{s,i}(t)$ and $T_{s,o}(t)$, respectively. The reason

for this distinction is that the inside shell surface temperature is relevant for the radiation heat exchange with the passengers, as explained in the comfort model below. Finally, the RHs are modeled as surfaces with a uniform temperature $T_{rh}(t)$.

The HVAC system that is used to provide thermal comfort for the passengers consists of an air heating and cooling unit and RHs, which are electrically heated surfaces at a temperature T_{rh} . The RHs increase the thermal comfort by directly heating passengers via radiation, without significantly increasing the air temperature [32]. Lastly, air curtains are also considered, which can reduce the losses through open doors. The inputs to the HVAC system can be summarized as follows:

$$\mathbf{u}(t) = (P_{hc}(t), P_{rh}(t), u_{hc}(t), u_{aircirt}(t), u_{rh}(t)), \quad (1)$$

where $P_{hc}(t)$ and $P_{rh}(t)$ denote the power provided to the air heating and cooling unit and the RHs, respectively. The integer variable $u_{hc}(t)$ is used to define the operating mode of the air heating and cooling unit:

$$u_{hc}(t) = \begin{cases} 1 & \text{heating,} \\ 0 & \text{passive,} \\ -1 & \text{cooling.} \end{cases} \quad (2)$$

The binary variables $u_{aircirt}(t)$ and $u_{rh}(t)$ are used to enable or disable the air curtains and the RHs, respectively. The total power consumption of the HVAC system is given by

$$P_{hvac}(t) = P_{hc}(t) + P_{rh}(t) + P_{aircirt}(t), \quad (3)$$

where $P_{aircirt}(t)$ denotes the power consumption of the air curtains.

The thermal model is subject to various disturbances, which are summarized in the vector

$$\mathbf{d}(t) = (T_{\infty}(t), I_{dni}(t), I_{dhi}(t), t, N_{pass}(t), \zeta_{door}(t)). \quad (4)$$

The uniform ambient temperature $T_{\infty}(t)$, the direct normal irradiance (DNI) $I_{dni}(t)$, and the diffuse horizontal irradiance (DHI) $I_{dhi}(t)$ characterize the meteorological conditions, which influence the various heat gains and losses shown in Figure 1. The time variable t denotes an absolute point in time. It is explicitly included in the disturbance vector, since it is used to calculate solar angles and shadow factors further below. The number of passengers $N_{pass}(t)$ and the fraction of open doors $\zeta_{door}(t)$ influence metabolic heating rate and the door losses, respectively.

In the following subsections, we first introduce the models for all the heat flows and then state the system of ordinary differential equations (ODEs) that describe the temperature dynamics.

2.1.1. Convection, Conduction, Radiation

The modeled temperature differences lead to convective, conductive, and radiative heat exchange. We apply Newton's law of cooling to obtain the convective heat transfer between the shell and cabin air, the interior and cabin air, the shell and

ambient, and the RHs and cabin air, respectively:

$$\dot{Q}_{h,s,i}(t) = h_{in} \cdot A_s \cdot (T_{cab}(t) - T_{s,i}(t)), \quad (5)$$

$$\dot{Q}_{h,int}(t) = h_{in} \cdot A_{int} \cdot (T_{int}(t) - T_{cab}(t)), \quad (6)$$

$$\dot{Q}_{h,s,o}(t) = h_{out} \cdot A_s \cdot (T_{s,o}(t) - T_{\infty}(t)), \quad (7)$$

$$\dot{Q}_{h,rh}(t) = h_{rh} \cdot A_{rh} \cdot (T_{rh}(t) - T_{cab}(t)). \quad (8)$$

The values for the convective heat transfer coefficients at the RHs h_{rh} , inside h_{in} , and outside h_{out} are based on the norm [38] and are adjusted for increased air movement inside the cabin and an average bus velocity of 15 km h⁻¹. The surface area of the hull A_s is given by the cabin dimensions (l_{cab} , w_{cab} , h_{cab}). The RH surface area A_{rh} is given by the single panel size and by assuming a distribution of 16 panels on the ceiling of the cabin [32]. We tune the interior surface area A_{int} to reproduce heat-up and cool-down trajectories generated with a three-dimensional simulation model implemented in a high-fidelity simulator.

For the conductive heat transfer through the shell, we again use Newton's law of cooling, i.e.,

$$\dot{Q}_k(t) = k_s \cdot A_s \cdot (T_{s,i}(t) - T_{s,o}(t)), \quad (9)$$

where k_s is the mean heat conductance through the bus enclosure. This value is calculated to match an overall U-value of 2.9 W m⁻² K⁻¹, which has been determined for a city bus in a climate chamber [39].

For simplicity, all surfaces are assumed to be perfect emitters and the windows are assumed to be opaque to infrared radiation [40]. Assuming a uniform ambient temperature, the heat emitted by the shell of the bus is given by

$$\dot{Q}_{r,s,o}(t) = \sigma \cdot A_s \cdot (T_{s,o}(t)^4 - T_{\infty}(t)^4), \quad (10)$$

where σ is the Stefan-Boltzmann constant. In the bus cabin, radiative exchange occurs between the RHs, the shell, and the interior. To characterize this exchange, we need the view factors between these surfaces [40]. Since the RHs are mounted in a coplanar arrangement on the ceiling, their mutual view factor is zero. Furthermore, without specifying a specific geometry, we assume that the view factor from the interior to itself is negligible. For the view factor from the RHs to the interior, we assume a value of $F_{rh \rightarrow int} = 30\%$. By applying the "summation" and "reciprocity" rules [40], we can then determine both the values of the view factors from the RHs to the shell $F_{rh \rightarrow s,i}$ and from the interior to the shell $F_{int \rightarrow s,i}$. Finally, the radiative heat exchange between the RHs and shell, RHs and interior, and interior and shell, respectively, is calculated as:

$$\dot{Q}_{r,rh \rightarrow s,i}(t) = \sigma \cdot A_{rh} \cdot F_{rh \rightarrow s,i} \cdot (T_{rh}(t)^4 - T_{s,i}(t)^4), \quad (11)$$

$$\dot{Q}_{r,rh \rightarrow int}(t) = \sigma \cdot A_{rh} \cdot F_{rh \rightarrow int} \cdot (T_{rh}(t)^4 - T_{int}(t)^4), \quad (12)$$

$$\dot{Q}_{r,int \rightarrow s,i}(t) = \sigma \cdot A_{int} \cdot F_{int \rightarrow s,i} \cdot (T_{int}(t)^4 - T_{s,i}(t)^4). \quad (13)$$

2.1.2. Door Losses

To estimate the buoyancy-induced air exchange through opened doors, we use a model based on Bernoulli's law and

the ideal gas law [41]. Based on the air exchange, we can calculate the corresponding heat losses through the doors with height h_{door} and a combined overall width $w_{door,tot}$ as follows:

$$\dot{Q}_{door}(t) = \frac{\rho_{air} \cdot C_d \cdot \sqrt{g \cdot h_{door}^3} \cdot w_{door,tot}}{3} \cdot \sqrt{\frac{|T_{cab}(t) - T_{\infty}(t)|}{T_{\infty}(t)}} \cdot (T_{cab}(t) - T_{\infty}(t)) \cdot c_{p,air} \cdot \zeta_{door}(t) \cdot (1 - \zeta_{aircurt} \cdot u_{aircurt}(t)), \quad (14)$$

where ρ_{air} denotes the air density, g denotes the gravitational acceleration, and C_d denotes an empirical discharge coefficient [41]. The fraction $\zeta_{door}(t)$ denotes the fraction of the doors that are open. For instance, $\zeta_{door}(t) = 1$ means all doors are open. The final term concerns the air curtains, which are activated with the binary variable $u_{aircurt}(t)$, and reduce the losses by a constant fraction $\zeta_{aircurt}$, the value of which is based on [29, 41].

The air curtain power requirement is given by

$$P_{aircurt}(t) = u_{aircurt}(t) \cdot \zeta_{door}(t) \cdot P_{aircurt,0}, \quad (15)$$

where the power consumption of the blowers $P_{aircurt,0}$ is based on measurements on a single door in an experimental study that features a comparable vehicle [42]. The power requirement of the air curtains is zero if they are disabled (i.e., $u_{aircurt}(t) = 0$) or if the doors are closed (i.e., $\zeta_{door}(t) = 0$).

2.1.3. Solar Heat Gain

For the calculation of the solar heat gain, we consider both direct and diffuse irradiation. The solar altitude angle $\beta(t)$ can be calculated based on the local coordinates and the datetime [43]. Based on the DNI denoted by $I_{dni}(t)$ and DHI denoted by $I_{dhi}(t)$, the mean irradiance on the roof and on the wall can be calculated as

$$I_{roof}(t) = \cos\left(\frac{\pi}{2} - \beta(t)\right) \cdot I_{dni}(t) + I_{dhi}(t), \quad (16)$$

$$I_{wall}(t) = \frac{\cos(\beta(t))}{\pi} \cdot I_{dni}(t) + \frac{1}{2} \cdot I_{dhi}(t), \quad (17)$$

where the latter is calculated based on the assumption that the bus is driving in all directions with equal probability [32].

Based on the irradiance values, the total heat gain on the outside shell of the cabin is given by

$$\dot{Q}_{sol,s,o}(t) = (1 - \zeta_{sh}(t)) \cdot (A_{roof} \cdot I_{roof}(t) \cdot \alpha_{paint} \cdot (1 - \zeta_{roof}) + A_{wall} \cdot I_{wall}(t) \cdot (1 - \zeta_{win}) \cdot \alpha_{paint}), \quad (18)$$

where A_{roof} and A_{wall} denote the roof surface area and the combined surface area of all walls, respectively. The surfaces of the bus hull are painted in bright colors and their solar absorptivity is denoted by α_{paint} , which is estimated based on data published in [40]. The fractions ζ_{roof} and ζ_{win} denote the fraction of the roof that is shaded by components such as batteries, and the fraction of the walls that are windows, respectively. For the fraction $\zeta_{sh}(t)$, which represents the fraction of time in which the bus is in the shade, we have developed a simulation in geographic information system (GIS) software to calculate the portion of the road along a route in Zürich that is shaded according to a

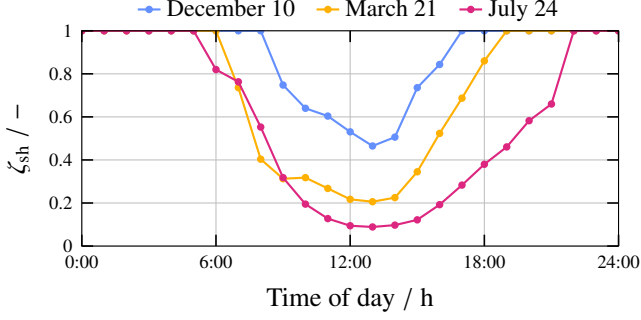


Figure 2: Shadow fraction ζ_{sh} averaged over a specific bus route in Zürich, based on a simulation using GIS software and a three-dimensional model of the city of Zürich [44, 45].

three-dimensional model of the city, including buildings and trees [44], and topography [45]. The model is then evaluated for every full hour over an entire year. We use linear interpolation between the calculated values to determine the value of the shadow fraction $\zeta_{sh}(t)$ at any specific point in time. Some sample results of this process are shown in Figure 2.

A part of the radiation hitting the windows is assumed to be transmitted into the cabin, characterized by the solar transmissivity τ_{win} of the windows, whose value is given by the manufacturer. The solar radiation transmitted into the bus through the windows is assumed to be fully absorbed by either the interior or the inside shell. The corresponding heat flows are:

$$\dot{Q}_{sol,int}(t) = (1 - \zeta_{sh}(t)) \cdot A_{wall} \cdot I_{wall}(t) \cdot \zeta_{win} \cdot \tau_{win} \cdot \zeta_{int}, \quad (19)$$

$$\dot{Q}_{sol,s,i}(t) = (1 - \zeta_{sh}(t)) \cdot A_{wall} \cdot I_{wall}(t) \cdot \zeta_{win} \cdot \tau_{win} \cdot (1 - \zeta_{int}), \quad (20)$$

where we assume that $\zeta_{int} = 30\%$ is absorbed by the interior.

2.1.4. Heat Sources

The power provided to the RHs is denoted by $P_{rh}(t)$, which we assume to be fully converted into heat. Furthermore, we assume that the RHs are insulated against the ceiling.

In steady state, the heat provided by the air heating and cooling unit can be calculated based on the unit's coefficient of performance (COP) $\gamma(t)$:

$$\dot{Q}_{hc,ss}(t) = u_{hc}(t) \cdot \gamma(t) \cdot P_{hc}(t), \quad (21)$$

where the mode selection $u_{hc}(t)$ determines the sign of the heat flow, as introduced in (2). For purely resistive heating (e.g., with positive temperature coefficient (PTC) elements), the COP is $\gamma(t) = 1$ in heating mode. For heating based on an HP and for cooling, the modeled COP depends on the temperature difference between the two thermal reservoirs. The corresponding dependency, as shown in the top left plot of Figure 3, is fitted to measurement data of various operating points provided by the vapor compression cycle (VCC) manufacturer. This fit achieves an R^2 value of more than 90%.

Due to the thermal dynamics of the VCC, as well as the dynamics of the low-level controller of the expansion valve, the heat flow of an HP or an air conditioning (AC) system does not

change instantaneously when the compressor power $P_{hc}(t)$ is changed. For simplicity, we model these dynamics by filtering the steady-state values $\dot{Q}_{hc,ss}(t)$ as given in (21) with a first-order element, similarly to, e.g., [46]. This results in an ODE for the heat provided by the air heating and cooling unit:

$$\frac{d}{dt} \dot{Q}_{hc}(t) = \frac{1}{\tau_{vcc}} \cdot (\dot{Q}_{hc,ss}(t) - \dot{Q}_{hc}(t)). \quad (22)$$

Based on a physical simulation of a VCC, we have determined a time constant $\tau_{vcc} = 20$ s to be a reasonable value, which is slightly longer than what is observed in units for passenger cars [47, 48].

By assuming that the heat supplied by the air heating and cooling unit is fully transferred into the cabin air, we implicitly assume that the unit is operated in recirculation mode, which is a reasonable assumption for city buses, where the air exchange through open doors typically provides enough fresh air to maintain sufficient cabin air quality.

The heat emitted by $N_{pass}(t)$ passengers is modeled as

$$\dot{Q}_{pass}(t) = N_{pass}(t) \cdot \dot{Q}_{met}, \quad (23)$$

where \dot{Q}_{met} denotes the average metabolic heat rate of a human when seated [49]. Lastly, all other heat sources (electric components, lights, screens) are captured by a constant heat flow \dot{Q}_{other} .

2.1.5. Thermal Reservoirs

Based on the first law of thermodynamics and the heat flows shown in Figure 1, we can formulate the following system of ODEs for the five thermal reservoirs:

$$\frac{d}{dt} T_{rh} = \frac{1}{C_{rh}} (P_{rh} - \dot{Q}_{h,rh} - \dot{Q}_{r,rh \rightarrow int} - \dot{Q}_{r,rh \rightarrow s,i}), \quad (24a)$$

$$\frac{d}{dt} T_{int} = \frac{1}{C_{int}} (\dot{Q}_{sol,int} + \dot{Q}_{r,rh \rightarrow int} - \dot{Q}_{h,int} - \dot{Q}_{r,int \rightarrow s,i}), \quad (24b)$$

$$\frac{d}{dt} T_{cab} = \frac{1}{C_{cab}} (\dot{Q}_{pass} + \dot{Q}_{other} + \dot{Q}_{hc} + \dot{Q}_{h,rh} + \dot{Q}_{h,int} - \dot{Q}_{h,s,i} - \dot{Q}_{door}), \quad (24c)$$

$$\frac{d}{dt} T_{s,i} = \frac{1}{C_{s,i}} (\dot{Q}_{h,s,i} + \dot{Q}_{sol,s,i} + \dot{Q}_{r,rh \rightarrow s,i} + \dot{Q}_{r,int \rightarrow s,i} - \dot{Q}_k), \quad (24d)$$

$$\frac{d}{dt} T_{s,o} = \frac{1}{C_{s,o}} (\dot{Q}_k + \dot{Q}_{sol,s,o} - \dot{Q}_{h,s,o} - \dot{Q}_{r,s,o}), \quad (24e)$$

where we omit the time dependencies of the temperature and heat flow variables to increase readability.

We estimate the heat capacity of the RHs C_{rh} based on dimensions and manufacturer's specifications. The heat capacity of the cabin air C_{cab} is calculated based on the cabin volume V_{cab} , as

$$C_{cab} = \rho_{air} \cdot c_{p,air} \cdot V_{cab}. \quad (25)$$

The values of the heat capacity for the interior C_{int} , the shell inside $C_{s,i}$, and outside $C_{s,o}$ are determined to reproduce heat-up and cool-down trajectories as mentioned above.

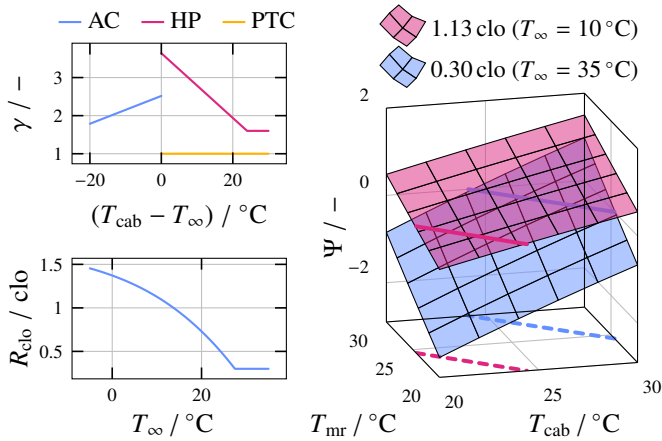


Figure 3: Visualization of the temperature-dependent model components. The solid lines in the right plot correspond to the temperature values representing a thermally neutral environment ($\Psi(t) = 0$). The dashed lines are the corresponding projections onto the ground plane, for clarity.

2.2. Comfort

We model thermal comfort according to the norm [49], which characterizes the thermal comfort in terms of the predicted mean vote (PMV), ranging from -3 (“cold”) to $+3$ (“hot”). This model has been originally proposed by Fanger [50] and is the most widely used for bus cabins [51]. For our calculations, we assume a constant air velocity $v_{\text{cab}} = 0.1 \text{ m s}^{-1}$ and a constant relative humidity of $\phi_{\text{cab}} = 40\%$. For the metabolic heat rate, we use $\dot{Q}_{\text{met}} = 125.3 \text{ W}$, which corresponds to a value of 1.2 met. Thus, the PMV is calculated according to [49] as a function of the air temperature $T_{\text{cab}}(t)$, the mean radiant temperature $T_{\text{mr}}(t)$, and the clothing insulation factor $R_{\text{clo}}(T_{\infty}(t))$, i.e.:

$$\Psi(t) = f(T_{\text{cab}}(t), T_{\text{mr}}(t), R_{\text{clo}}(T_{\infty}(t)), v_{\text{cab}}, \phi_{\text{cab}}, \dot{Q}_{\text{met}}). \quad (26)$$

Two sample visualizations of this dependency are shown in the right plot of Figure 3. The insulation factor $R_{\text{clo}}(T_{\infty}(t))$ quantifies the clothing of the passengers, which depends on the ambient temperature [52]. We use the same dependency as in a previous study [32], shown in the bottom left plot of Figure 3.

To determine the mean radiant temperature $T_{\text{mr}}(t)$, we describe a passenger by an upright cuboid with the dimensions $0.25 \text{ m} \times 0.25 \text{ m} \times 1.7 \text{ m}$, which does not take part in the radiation balance of the enclosure. The passenger can thus be considered a “passive” sensory device, apart from its metabolic heat release described by (23). As passenger placement is typically not recorded, we use a randomized approach for passenger placement in our model. For a visualization of such a distribution, we refer to our previous publication [32]. Again, using the view factor relations given in [40], the mean radiant temperature of a passenger is denoted by

$$T_{\text{mr}}(t)^4 = \frac{1}{\sum_i A_i} \cdot \left(T_{\text{rh}}(t)^4 \cdot \sum_i (A_i \cdot F_{i \rightarrow \text{rh}}) + T_{\text{s},i}(t)^4 \cdot \sum_i (A_i \cdot F_{i \rightarrow \text{s},i}) + T_{\text{int}}(t)^4 \cdot \sum_i (A_i \cdot F_{i \rightarrow \text{int}}) \right) \quad (27)$$

where the index i is used to iterate over the five surfaces of the cuboid. The view factors to the RHs, $F_{i \rightarrow \text{rh}}$, can be determined analytically, as explained in [53]. For the view factors to the interior, we assume $F_{i \rightarrow \text{int}} = 30\%$. The view factor to the shell, $F_{i \rightarrow \text{s},i}$, can then be found using the summation rule [40]. Finally, to obtain an overall estimate of the PMV for all passengers, we average the respective PMV values as calculated in (26).

2.3. Data Sources

The numerical data needed to characterize the disturbances $\mathbf{d}(t)$ is collected from multiple sources. The operating schedule, the passenger load, and the door openings are obtained from the ZTBus dataset [54], where we use the data for bus number 183. Concerning door openings, the ZTBus dataset only contains information of whether at least one door is open. Our analysis of log data from a similar vehicle reveals that, on average, about 60% of the four doors open at each stop. We include this factor of 60% into the pre-processing of $\zeta_{\text{door}}(t)$ for all the simulations. All meteorological data are obtained from a meteorological station of the Swiss Federal Office of Meteorology and Climatology (MeteoSwiss) located in Zürich.

Figure 4 shows an example of the disturbances, recorded on a summer day. An example of a winter day is shown in Figure 6 in the results section.

2.4. Steady-State Approximation

The dynamic thermal model introduced in the previous subsections can be simplified based on the principle of timescale separation. For our system, this principle means that the dynamics of the ODEs (22), (24) can be neglected (i.e., all time derivatives are set to zero) if the typical rate of change of the disturbances $\mathbf{d}(t)$ is significantly lower than the characteristic response time of the system¹. In that case, the disturbances can be assumed constant over a certain period of time, and the resulting system of nonlinear equations can be evaluated using a suitable numerical method. To accommodate for changes in the disturbances, this evaluation can be repeated with a representative sample of (constant) disturbances. For instance, instead of simulating the entire time-resolved trajectory of around 14 h shown in Figure 4, the nonlinear system of equations can be evaluated 14 times, if hourly averages for each of the disturbances are used as representative samples. The resulting performance metrics, such as the HVAC system power consumption, can then be averaged to obtain an approximation of the corresponding dynamic performance. Such an approximation requires much less computation than the corresponding dynamic simulation.

Looking at the disturbances shown in Figure 4, we observe that the ambient temperature and both types of solar irradiance change only slowly and can thus be assumed constant during one hour. Changes in the number of passengers and door openings, on the other hand, happen on a timescale very similar to or faster than the characteristic response time of the thermal dynamics, which is in the order of around 10 min [15, 16]. In other words,

¹For a first-order, linear time-invariant system, this would be the time constant.

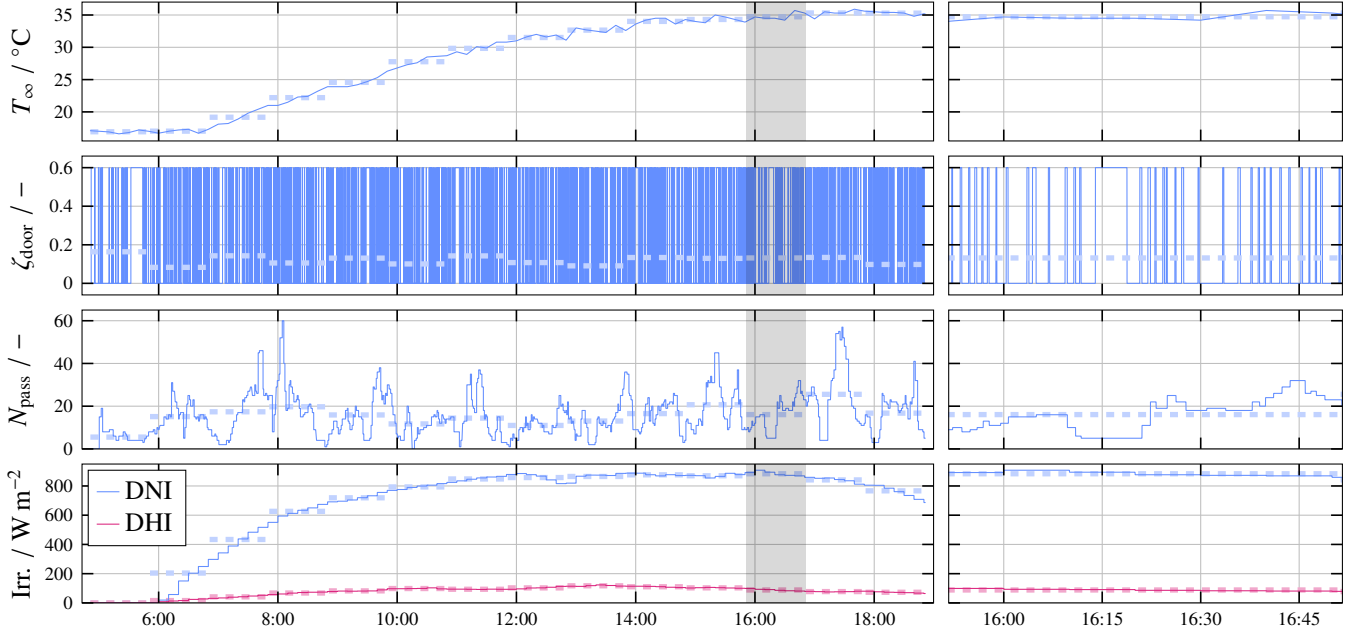


Figure 4: Disturbances $\mathbf{d}(t)$ on a summer day, recorded on 2019-07-24. Thin solid lines represent the time-resolved data, while thick dashed lines represent hourly averages. The shaded segment is the basis for the visualization in Figure 10. The plots shown on the right are a zoomed version of this segment.

there is no clear timescale separation for these disturbances and a steady-state approximation cannot represent the dynamic operation of the HVAC subject to these disturbances. However, as the cabin temperature is typically closed-loop controlled, we can assume that these disturbances are rejected by the corresponding controller. Hence, we use the steady-state approximation to evaluate the *average* operation of the *closed-loop controlled* HVAC system. The accuracy of this approximation is evaluated below in Section 4.1.

3. Optimal HVAC Operation

Optimizing the HVAC operation based on a dynamic thermal model is typically a challenging and computationally intensive task. It involves the formulation of an optimal control problem (OCP), which can be transcribed to a non-linear program (NLP), which is then solved using a suitable method. As the sampling time must be small enough to capture the dynamics, but the driving missions are typically very long, the number of optimization variables in such an NLP is large. Therefore, the computation time to solve such problems is high, especially if they involve integer decision variables such as $u_{hc}(t)$, $u_{aircirt}(t)$, and $u_{rh}(t)$. This prohibits the evaluation of year-round performance within a reasonable time frame. Conversely, optimizing the HVAC operation based on the steady-state approximation described in Section 2.4 can be accomplished by formulating a comparably small NLP. As this involves much less optimization variables, the solution can be computed much quicker, which enables the evaluation of year-round performance. In this section, we formulate such an optimization problem and explain how it can be solved efficiently.

3.1. Problem Formulation

The objective is to minimize the total power consumption P_{hvac} given by (3) for a given set of averaged disturbances \mathbf{d} while respecting a specified comfort requirement. This can be mathematically formulated as follows:

$$\underset{\mathbf{u}}{\text{minimize}} \quad P_{hvac}, \quad (28a)$$

$$\text{s.t.} \quad (22), (24) \text{ in steady state}, \quad (28b)$$

$$\Psi \in [\Psi_{\min}, \Psi_{\max}], \quad (28c)$$

$$0 = u_{rh} \cdot (T_{rh} - T_{rh,target}), \quad (28d)$$

$$0 = (1 - u_{rh}) \cdot P_{rh}, \quad (28e)$$

where (28c) defines the comfort requirement in the form of a box constraint on the PMV. Depending on the value of the binary variable u_{rh} , one of the two vanishing constraints, (28d) and (28e), is trivially satisfied, while the other constraint is “activated”: If the RHs are used, i.e., $u_{rh} = 1$, the RH temperature is constrained by (28d) according to the data sheet. If they are disabled, i.e., $u_{rh} = 0$, the corresponding power must be zero as enforced by (28e). This formulation prevents solutions where the RHs are operated outside of their specifications. We omit all time dependencies in (28) to highlight the fact the the system is assumed to be in steady state.

3.2. Solution Approach

The optimization problem (28) presents three challenges for numerical solution algorithms. In this section, we show how we address these challenges.

First, we address the three integer optimization variables u_{hc} , u_{rh} , and $u_{aircirt}$. To optimize the operating mode, we introduce

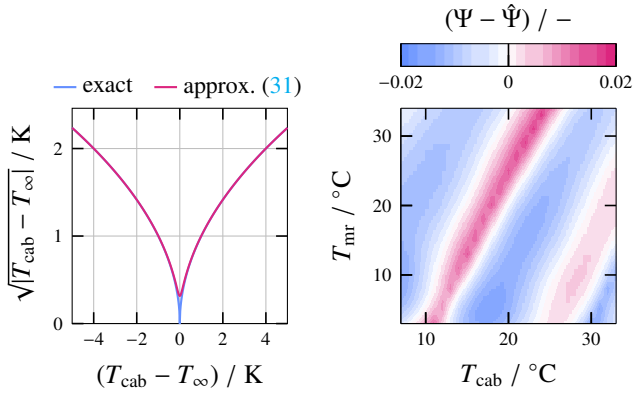


Figure 5: Visualizations of the model approximations. The left plot shows the approximation (31). The right contour plot shows the error of the approximation (32) for an ambient temperature of $T_{\infty} = 10^{\circ}\text{C}$.

two lifting variables to represent the bidirectional heat provided by the air heating and cooling unit as

$$\dot{Q}_{hc} = \dot{Q}_{heat} + \dot{Q}_{cool}, \quad (29)$$

where $\dot{Q}_{heat} > 0$ denotes the heat provided by the heating system and $\dot{Q}_{cool} < 0$ denotes the heat removal by the AC system. In steady state, the ODE (22) trivially resolves to $\dot{Q}_{hc} = \dot{Q}_{hc,ss}$. Hence, using the two lifting variables and (21), the air heating and cooling power conversion can be reformulated as follows:

$$P_{hc} = \frac{\dot{Q}_{heat}}{\gamma_{hp}} - \frac{\dot{Q}_{cool}}{\gamma_{ac}}, \quad (30)$$

where γ_{hp} and γ_{ac} denote the COP for heating and cooling, respectively (see Figure 3). Although this reformulation allows simultaneous heating and cooling, the optimization algorithm will avoid such suboptimal behavior. The two binary decision variables $u_{aircirt}$ and u_{rh} are eliminated by solving the continuous optimization problem for each of the four combinations of these variables and selecting the solution with the lowest objective value.

Second, the model of the door losses given by (14) is non-smooth in the variable T_{cab} . Such non-smoothness often leads to numerical issues when using derivative-based optimization methods. For this reason, we replace the square root in (14) by a smooth approximation:

$$\sqrt{|T_{cab} - T_{\infty}|} \approx \sqrt[4]{(T_{cab} - T_{\infty})^2 + 0.01}. \quad (31)$$

The value 0.01 results in good convergence behavior of the numerical method employed while keeping the error of the approximation low, as shown in the left plot of Figure 5.

Third, the relationship (26) is based on iterative calculations [49, 50]. As derivative-based optimization tools require closed-form expressions of all constraints, we use a feedforward artificial neural network (ANN) with a single hidden layer with five neurons and the hyperbolic tangent activation function to approximate this dependency:

$$\hat{\Psi} = f_{ann, T_{\infty}}(T_{cab}, T_{mr}). \quad (32)$$

The parameters of $f_{ann, T_{\infty}}(\cdot)$ are fitted for each value of $R_{clo}(T_{\infty})$, which is indicated by the subscript T_{∞} . The error of one of these approximations is visualized in the right plot of Figure 5. The mean absolute error (MAE) in this example is less than 0.01.

Based on these simplifications and reformulations, the optimization problem (28) can be formulated as a set of four NLPs. To solve these problems, we use the CasADi [55] interface to Ipopt [56] and the linear solver MUMPS [57]. On a standard laptop, each of the four NLPs can be solved in around 40 ms on average. In a previous publication [32], we have presented an alternative solution approach which is based on a root-finding algorithm.

4. Results

The result section is split into three subsections. First, we compare the results of the optimization based on the steady-state model to simulations of the full dynamic model. Second, we present two case studies to show how the approach can be useful for different purposes. In the first case study, we compare the year-round performance of different HVAC systems. In the second case study, we extract setpoints from the optimal solutions of the steady-state models and use these setpoints for a causal controller in a dynamic simulation environment.

4.1. Validation of the Steady-State Assumption

In this subsection, we compare the results obtained by the approach based on optimizations of the steady-state model outlined in Section 3 to results obtained by performing a simulation of the dynamic thermal model introduced in Section 2.1. Thereby, we show that the steady-state model can be used to estimate the average performance of the closed-loop controlled HVAC system of a city bus. The following steps outline how the results shown in the subsequent figures are obtained:

1. We split the driving mission into segments of one hour length. We calculate the average values for the disturbances $\mathbf{d}(t)$ in each of these segments to obtain a set of samples each representing one hour of the original mission.
2. We optimize the HVAC operation in steady-state based on the approach presented in Section 3 for each of the samples.
3. We perform a dynamic simulation for the same mission. We use the results of the steady-state optimizations within the corresponding 1 h-segments as follows: The integer variables $u_{aircirt}$, u_{rh} , u_{hc} are directly used as constant inputs in a feed-forward manner in the corresponding 1 h-segment. The cabin temperature is used as a setpoint trajectory for a proportional-integral (PI) feedback controller which regulates $P_{hc}(t)$. Its proportional gain is 2000 W K^{-1} and its integral time constant is 100 s. For the initial conditions of all the temperatures, we use the bus depot temperature, which we assume to depend linearly on the ambient temperature:

$$T_{depot}(t) = (T_{\infty}(t) - 20^{\circ}\text{C}) \cdot 0.5 + 20^{\circ}\text{C}. \quad (33)$$

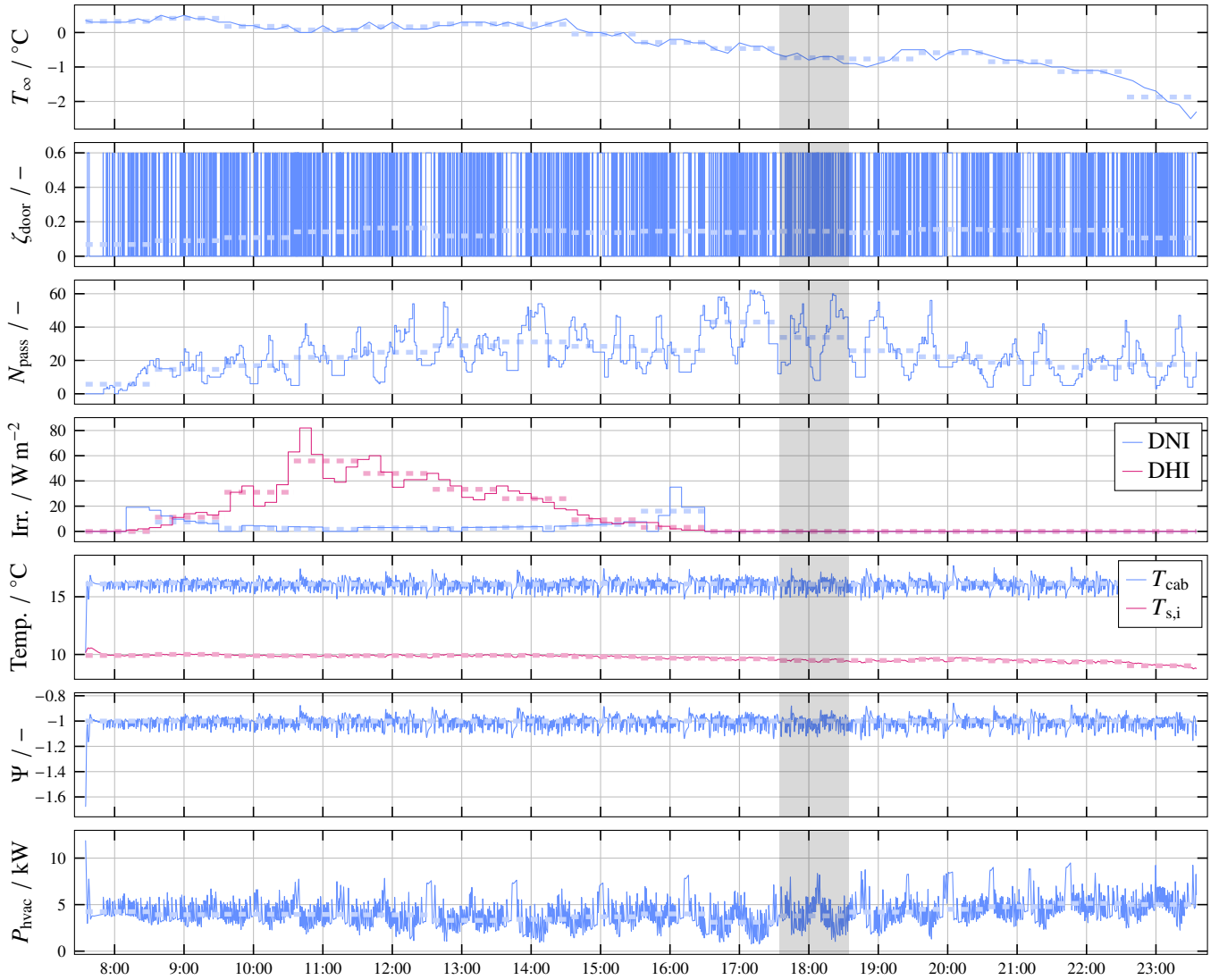


Figure 6: Full-day simulation of a winter day recorded on 2022-12-10. Thin solid lines represent dynamic simulation, while thick dashed lines represent the results of the steady-state approach proposed in this paper. The shaded segment is the basis for the visualization in Figure 9.

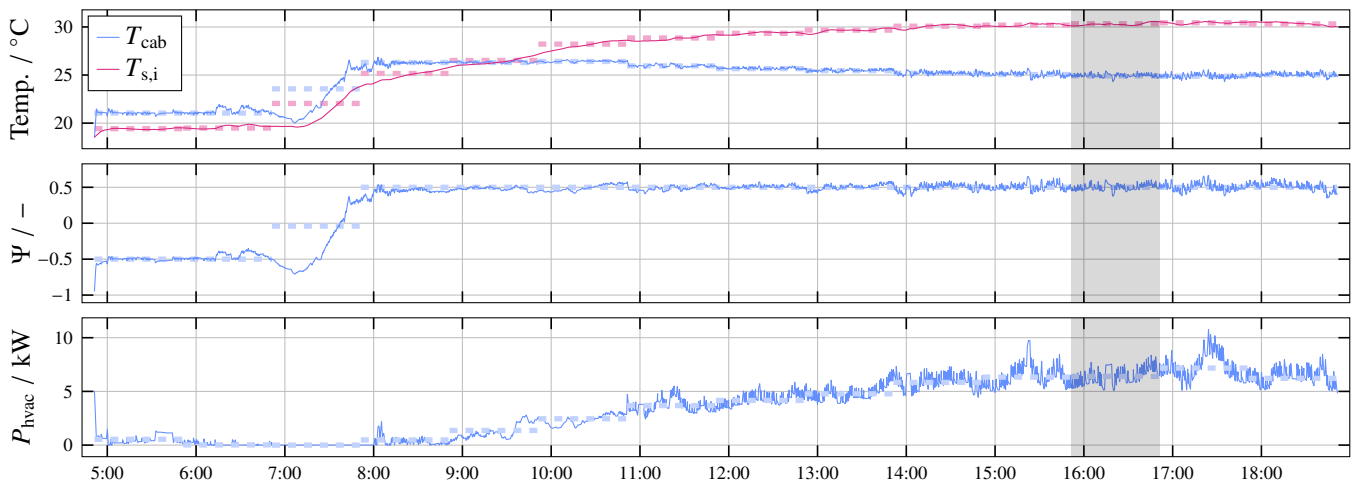


Figure 7: Full-day simulation of a summer day recorded on 2019-07-24, the disturbance trajectories of which are shown in Figure 4. Thin solid lines represent dynamic simulation, while thick dashed lines represent the results of the steady-state approach proposed in this paper. The shaded segment is the basis for the visualization in Figure 10.

Figure 6 shows the resulting trajectories of a full-day winter mission. The top four plots visualize the disturbances $\mathbf{d}(t)$. As the figure shows, the PI controller is able to track the cabin temperature $T_{\text{cab}}(t)$ well. The frequent door openings lead to significant disturbances in the overall heat balance, which cannot be fully compensated by the controller and are thus visible in short-term deviations from the target temperature. Even though only the cabin temperature is controlled, the shell inside temperature, which is also relevant for the thermal comfort, is shown to almost perfectly match the hourly values predicted by the steady-state solution. As the temperatures closely follow the steady-state solution, so does the PMV. While door openings lead to violations from the comfort requirement of $\Psi(t) \in [-1, +1]$, these violations are only short in duration and small in magnitude. The trajectory of $P_{\text{hvac}}(t)$ shows how slow disturbances, like changing solar irradiation or ambient temperature, lead to slow changes in the required power throughout the day, which are also present in the steady-state optimization. As the cabin temperature is controlled in closed loop, faster disturbances like varying passenger numbers lead to temporary deviations in $P_{\text{hvac}}(t)$ from the corresponding steady-state estimation.

Figure 7 shows a comparison for a full-day summer mission. The more demanding PMV requirement of $\Psi(t) \in [-0.5, +0.5]$ for this example is also satisfied reasonably well. The largest violation of the target PMV is observed after the mode switch from the “cooling” to the “passive” mode at around 06:50. Just after the switch to the “passive” mode, the PMV starts to drop below the lower limit of -0.5 . Hence, to satisfy the PMV requirements, the “heating” should have been active for a few more minutes. From this observation, we conclude that the ideal time instance for mode switches cannot be predicted accurately with the steady-state approach, as such a switch can only happen once per hour with this approach. In Section 4.3, we propose an improved method to handle mode switches in an online application. Door air curtains are only used after about 10:50, which is evident from the ripple effect appearing in $P_{\text{hvac}}(t)$ from that time onward.

Analogous simulations for both the winter and summer missions are performed with five different PMV constraints. The resulting performance values are visualized in Figure 8. Each data point in Figure 8, representing a pair of a dynamic and a static simulation, is a consolidation of entire simulation trajectories such as the ones shown in Figures 6 and 7. This consolidation is done based on the two primary performance indicators, i.e., the power consumption and the thermal comfort. The first performance indicator is represented by the mean power consumption

$$\bar{P}_{\text{hvac}} = \frac{1}{t_f - t_0} \cdot \int_{t_0}^{t_f} P_{\text{hvac}}(t') dt', \quad (34)$$

where t_0 and t_f represent the mission’s initial and final time, respectively. For the second performance indicator, we quantify the achieved PMV window by evaluating the maximum absolute value of the PMV trajectory. For the dynamic trajectories, we first smooth the PMV trajectory with a 15 min moving average filter, which corresponds to a typical dwell time of passengers in a city bus. Thus, this smoothed value represents an average

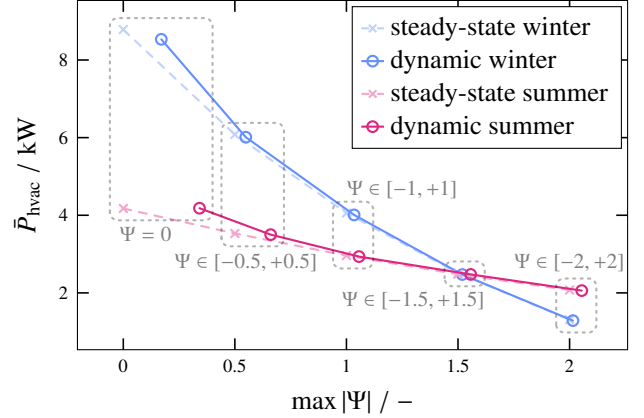


Figure 8: Comparison of Pareto fronts obtained using the steady-state approach and the dynamic simulation, for the summer and winter missions shown in Figures 6 and 7. The gray dotted boxes and corresponding labels denote the comfort range used to optimize the steady-state model.

comfort level experienced by passengers throughout a single ride. The maximum absolute value of this smoothed trajectory thus represents the single most uncomfortable trip of any passenger during the entire day. For this reason, we only consider PMV values when at least one passenger is present in the bus.

Figure 8 shows that the steady-state models are able to predict the behavior of the dynamic model with reasonable accuracy. The larger deviations in the winter mission for high comfort requirements can be attributed to the power limit of the HP of 12 kW. This limits the ability of the controller to compensate for the effect of prolonged door openings. As the door openings are averaged for the steady-state approach, such a temporary saturation does not influence the steady-state solution. However, as shown in the next subsection, temperatures below 0°C are relatively rare in Zürich. Thus, we do not expect this effect to significantly impact the annual performance metrics. The larger deviations in the summer mission can be attributed to the delayed mode switch, as observed in Figure 7 and explained above.

Figures 9 and 10 show example steady-state solutions from the winter and summer missions, respectively. These visualizations serve to provide some intuition on the range of temperature levels and heat flows that are present in the model.

4.2. Case Study 1: Offline Year-Round Evaluation

In this case study, we show how the steady-state optimization approach can be used to evaluate the year-round performance of different HVAC systems. For this purpose, we first provide an overview of the entire set of samples that we use to represent the year-round operation of the HVAC system. We then explain how we post-process the results to obtain representative annual performance metrics. Finally, we show the results of these calculations.

Based on the data sources introduced in Section 2.3, we create a dataset of constant disturbance values \mathbf{d} , consisting of 7399 samples, each of which represents the average values in a one-hour segment. Figure 11 provides an overview of this dataset.

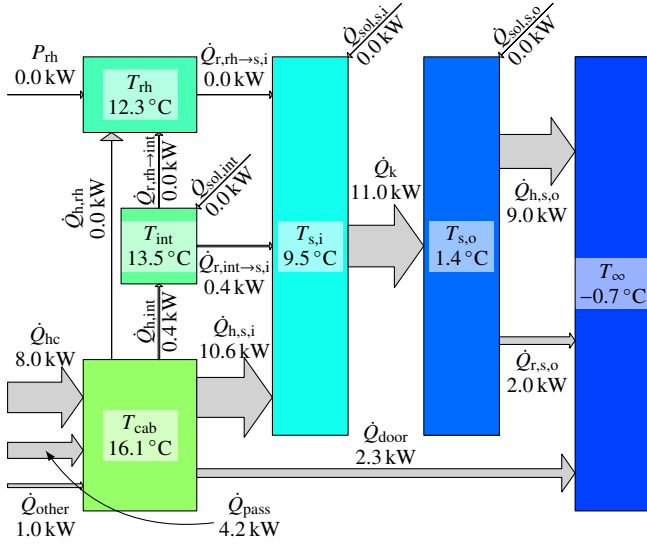


Figure 9: Visualization of the steady-state result corresponding to 2022-12-10 17:35 to 18:35, i.e., the shaded area in Figure 6. In this sample, a PMV of $\Psi = -1$ is reached. The arrow annotations represent the corresponding absolute values of the flows.

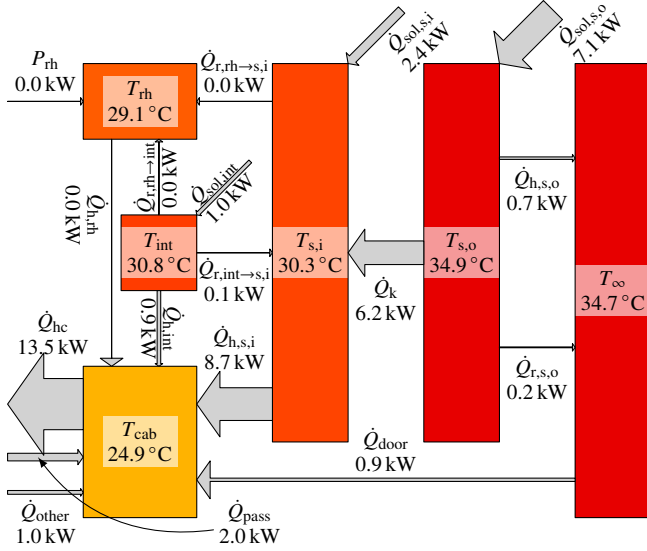


Figure 10: Visualization of the steady-state result corresponding to 2019-07-24 15:50 to 16:50, i.e., the shaded area in Figure 7. In this sample, a PMV of $\Psi = 0.5$ is reached. The arrow annotations represent the corresponding absolute values of the flows.

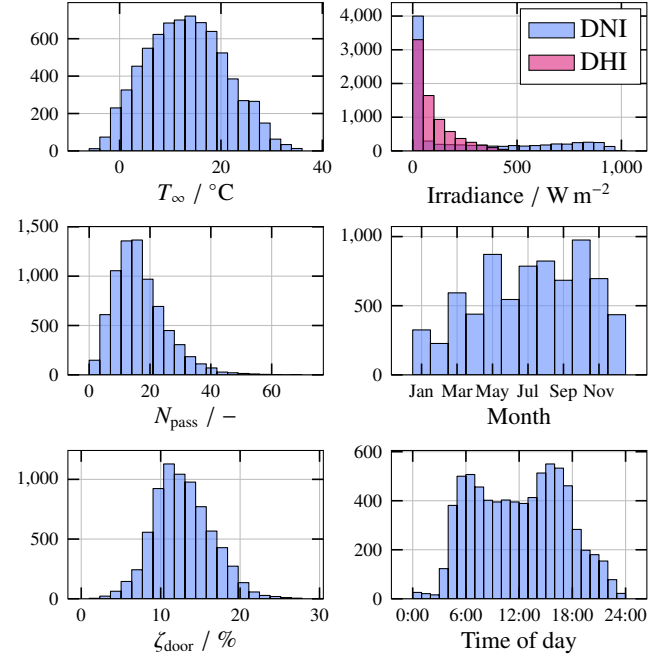


Figure 11: Distributions of the values of the disturbances in the 7399 samples.

As the samples are not uniformly distributed throughout the year, a simple time-average as introduced in (34) would not represent all seasons equally. Thus, we calculate a weighted mean of the results. Assuming sample i is recorded in January, for instance, we calculate its weight to be

$$w_{i,\text{jan}} = \frac{1}{325} \cdot \frac{31}{365}, \quad (35)$$

where the first factor represents the 325 samples in January (see Figure 11) and the second factor represents the weight of January with its 31 days in relation to the entire year. We use these weights to calculate the annual mean HVAC system consumption:

$$\check{P}_{\text{hvac}} = \sum_{i=1}^{N_{\text{samples}}} (w_i \cdot P_{\text{hvac},i}). \quad (36)$$

Such annual averages can be calculated for varying comfort requirements to obtain a Pareto front. Such a Pareto front quantifies how much a certain comfort requirement costs in terms of mean power consumption. Furthermore, it shows that increasing comfort levels becomes more and more expensive. Comparing the Pareto fronts for various HVAC designs, as shown in Figure 12, we observe that RHs can improve the mean energy efficiency of a PTC-based heating system by 5 to 7%. While an HP is a more expensive option, it also offers very significant benefits, with an annual reduction potential of 50 to 60%. Air curtains can further decrease the annual average consumption by 10 to 20%. As we have already shown in a previous study, a combination of an HP with RHs does not yield significant additional benefits [32].

For the most efficient HVAC system design, i.e., the HP with air curtains, we visualize the resulting PMV values in Figure 13 for multiple comfort requirements. Intuitively, whenever the

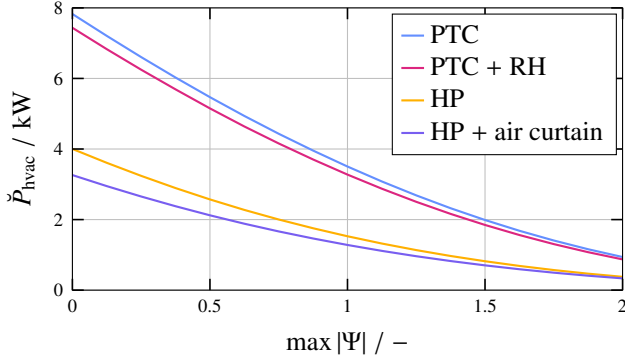


Figure 12: Pareto front for different HVAC system concepts showing the trade-off between the thermal comfort requirements and the mean annual power demand. This analysis is based on all 7399 samples.

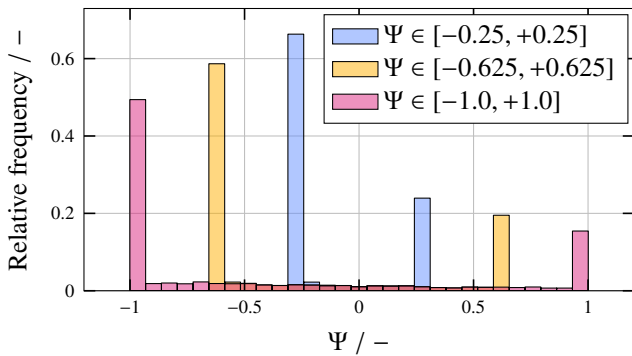


Figure 13: Overview of the optimized PMV values in all 7399 samples for varying comfort requirements. The results are based on the HVAC system with an HP and air curtains.

constraint on the PMV is active, the HVAC system consumes power to satisfy this constraint. For instance, Figure 13 shows that the lower PMV limit of $\Psi \geq -1$, is active in almost 50% of the samples. This means that heating is required almost 50% of the time to achieve this comfort requirement. Conversely, cooling is only required in less than 20% of the samples. This clearly demonstrates the fact that heating is the more relevant use case for the climatic conditions present in Zürich, despite the fact that January and February are slightly underrepresented in the samples considered in this case study.

4.3. Case Study 2: Causal Online Control

In this section, we show how the optimization results based on the approach presented in Section 3 can be used in an online controller without the need for predictive data. We do this by further focusing on the system with an HP and air curtains.

Most HVAC controllers used today track a cabin temperature setpoint, which in turn is typically dependent on the ambient temperature (see e.g. [19, 24, 28, 58]). Our suggestion is thus to use the results from all 7399 samples calculated in the previous section to generate such “setpoint profiles”, see Figure 14. Based on the shape of the point cloud, we use a quadratic fit for the heating profile and a piecewise linear fit for the cooling profile. We select conservative fits for both modes (i.e., we fit the profiles to the upper edge of the point cloud for heating and to the lower

edge for cooling) to maximize constraint satisfaction when the profiles are used. These profiles can then be tracked by the PI controller introduced in Section 4.1.

The heating and cooling setpoint profiles can also be used to determine the operating mode $u_{hc}(t)$ of the air heating and cooling unit. For this purpose, we propose a finite state machine, as illustrated in Figure 15. The constants of ± 1 K in this state machine were tuned manually, such that frequent mode changes are prevented.

To determine the usage of the air curtain, we visualize the mode decision in all 7399 samples in Figure 16. Based on this visualization, we determine a temperature difference threshold depending on the sign of $\dot{Q}_{hc}(t)$ (or equivalently, $u_{hc}(t)$, according to (21)), which are also visualized in Figure 16. Since these temperature thresholds turn out to be almost independent of the selected comfort criteria, we use the same values throughout all subsequent analyses.

Next, we conduct a dynamic simulation based on the driving mission recorded on 2019-07-24, i.e., the summer mission shown in Figures 4 and 7, as this mission features highly dynamic ambient conditions. We conduct multiple simulations to compare the temperature setpoints shown in Figure 14 with the corresponding setpoint profiles used in published literature, i.e., by Göhlich et al. [28] and by Hambræus and Minotta [58]. Figure 17 shows the resulting trajectories of four dynamic simulations with different temperature setpoint profiles. The setpoints are shown in the top plot, which qualitatively validates the respective tracking performance of the PI controller. The second and third plot show the achieved comfort values and the required total power, respectively. While the heuristic setpoints from the literature achieve varying comfort values throughout the day, the setpoints extracted from the left plots of Figure 14 are able to maintain a more consistent comfort range over the dynamically changing ambient conditions.

This observation is highlighted in Figure 18, which again shows the maximum absolute value of the PMV after being smoothed with a 15 min moving average filter. This figure shows that by extracting setpoints as shown in Figures 14 and 16 and using a causal controller, close-to-optimal performance is possible in terms of our performance indicators. Compared to heuristic setpoint profiles from the literature, our approach reaches a better comfort value more consistently, resulting in a better trade-off as shown in Figure 18. Furthermore, the systematic approach to extract these setpoints allows for the bus operator to freely choose specific comfort targets.

5. Conclusion

5.1. Contributions

In this paper, we have presented a dynamic thermal model of the passenger cabin and the HVAC system of a city bus, including a thermal comfort model. In a second step, we have introduced a steady-state approximation of this model. We have then demonstrated both how the steady-state model enables a simplified formulation of a mathematical program to optimize the HVAC system inputs and how it can be efficiently solved. We

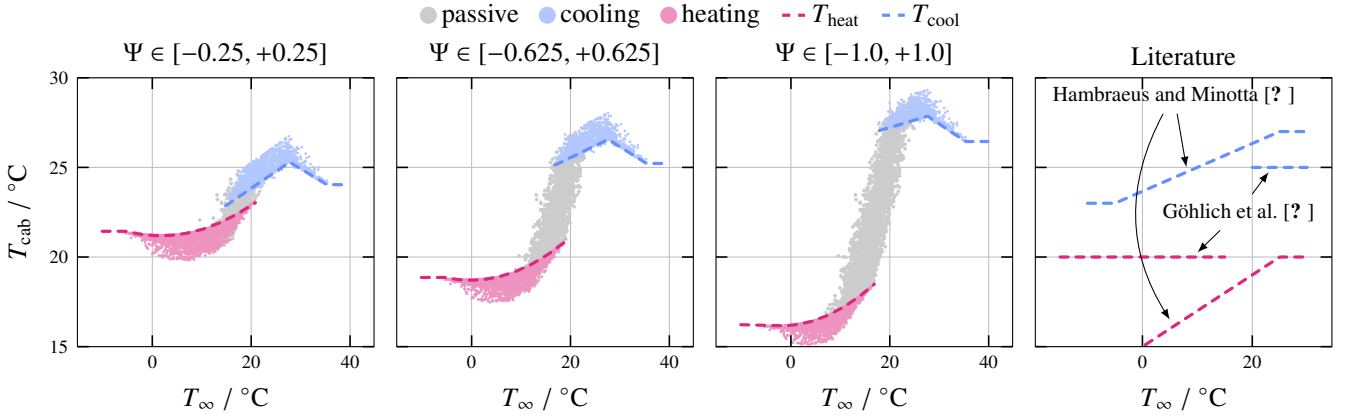


Figure 14: Visualization of the extracted temperature setpoint profiles for three different comfort requirements (left three plots). Each dot represents the result on one of the 7399 samples. The colors represent the active operating mode of the air heating and cooling unit. The right plot shows two setpoint profiles from published literature.

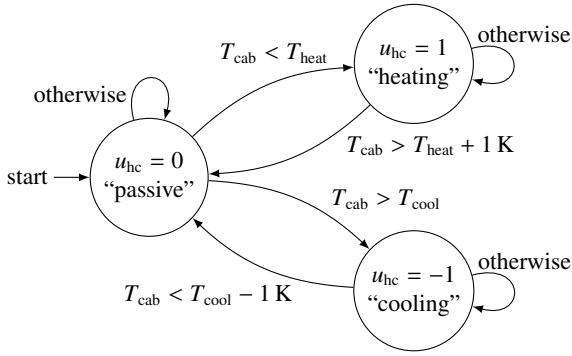


Figure 15: State machine to determine the operating mode u_{hc} of the air heating and cooling unit. Time dependencies are omitted to increase readability.

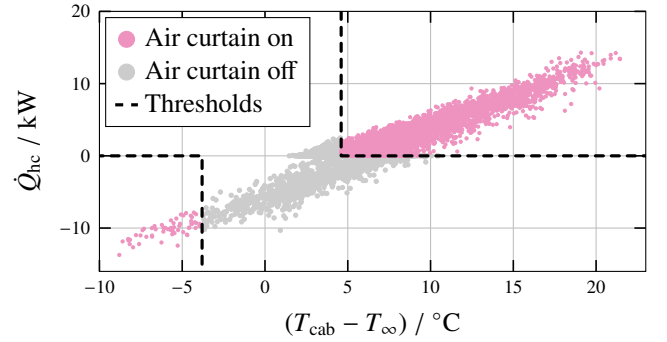


Figure 16: Visualization of the air curtain usage patterns. The black dashed lines visualize the two fitted thresholds for the heating mode ($\dot{Q}_{hc}(t) > 0$) and the cooling mode ($\dot{Q}_{hc}(t) < 0$), respectively. This visualization is based on a comfort requirement of $\Psi \in [-1, +1]$, but the extracted thresholds are almost identical for different requirements.

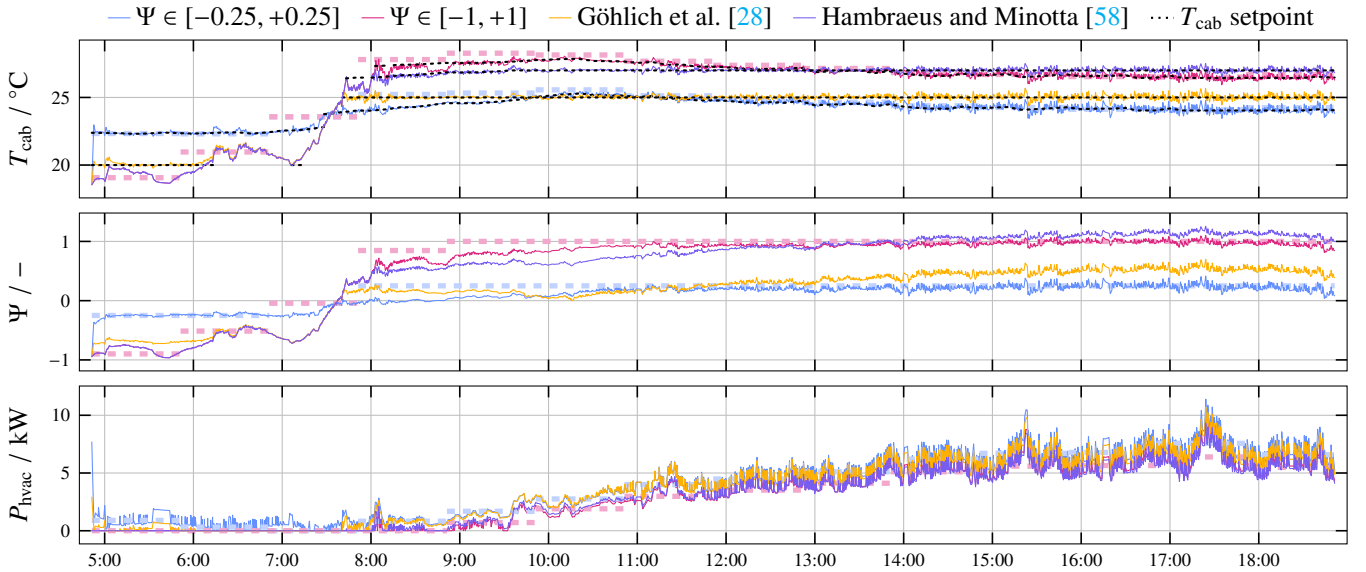


Figure 17: Simulation results for 2019-07-24 based on the setpoint profiles shown in Figures 14 and 16. Thin solid lines represent the dynamic results, while thick dashed lines represent the results of the steady-state optimization. The dotted black lines in the top plot represent the temperature setpoints if $u_{hc}(t) \in \{-1, 1\}$. The temperature setpoint is not defined if no heating or cooling is used (i.e., $u_{hc}(t) = 0$).

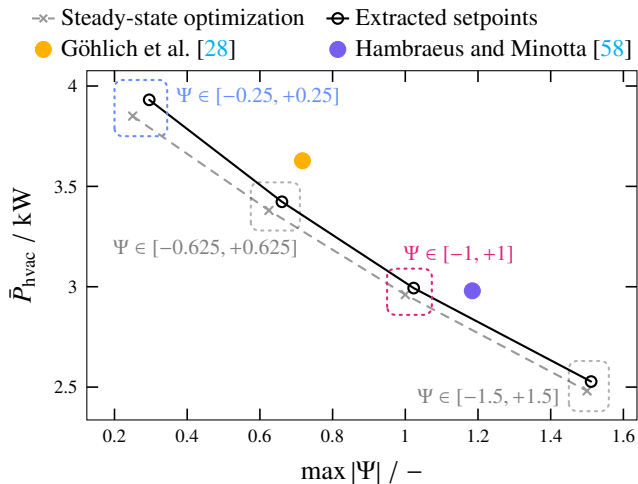


Figure 18: Comparison of the results predicted with the steady-state approach and the results obtained with causal controllers based on different temperature setpoint profiles. The dashed circles mark the solutions with the corresponding comfort requirements also shown in Figure 17.

have conducted a quantitative comparison between the dynamic and steady-state model. While a steady-state approximation of the HVAC system is not new in the context of public transportation vehicles (see e.g. [22, 23, 31, 32, 34]), this comparative analysis is a novel contribution. To showcase the practical usefulness of our methodology, we have conducted two case studies. In the first case study, we have compared the annual performance of various HVAC system configurations. In the second case study, we have illustrated how our results can be utilized to derive optimized setpoints for causal controllers.

5.2. Limitations and Outlook

While our study provides valuable insights, we see certain limitations and opportunities for future research. Although most of the presented model components are either validated or based on well-founded assumptions, a comprehensive validation of the entire thermal model is pending. To address this, a measurement campaign is planned with a prototype vehicle, which will be used to ensure the accuracy of the models.

Future research could explore additional factors related to passenger comfort, such as humidity, air quality, ventilation-induced draft, radiant asymmetry, or heated seats. Including these elements would further enrich the model and enable extended analyses of emerging trade-offs. Extending the objective to include investment costs or embodied emissions enables holistic comparisons of HVAC systems within frameworks like life-cycle costing (LCC) or life-cycle assessment (LCA). Conducting case studies for different climatic conditions would allow to identify optimal HVAC system configurations based on the deployment location. Lastly, future studies could also extend to case studies encompassing multiple types of public transportation vehicles, such as street cars and trains.

CRediT Authorship Contribution Statement

Fabio Widmer: Conceptualization, Methodology, Software, Validation, Visualization, Writing – original draft **Stijn van Dooren:** Conceptualization, Methodology, Validation, Visualization, Writing – review & editing **Christopher H. Onder:** Conceptualization, Funding acquisition, Project administration, Supervision

Declaration of Competing Interest

The authors declare that they have no known competing financial interests or personal relationships that could have appeared to influence the work reported in this paper.

Acknowledgments

This work was financially supported by the Swiss Federal Office of Energy (SFOE, contract number SI/502235). The industrial partners Carrosserie HESS AG and Verkehrsbetriebe Zürich (VBZ) provided assistance during data collection, model formulation, and validation. None of the partners played a role in the writing of the article.

References

- [1] J. Lang, C. Hyslop, N. Lutz, R. Black, P. Chalkley, T. Hale, F. Hans, N. Hay, N. Höhne, A. Hsu, T. Kuramochi, S. Mooldijk, S. Smith, *Net zero tracker*, Energy and Climate Intelligence Unit, Data-Driven EnviroLab, NewClimate Institute, Oxford Net Zero (2023). URL <https://zerotracker.net>
- [2] H. Ritchie, M. Roser, *Transport*, Our World in Data (2021). URL <https://ourworldindata.org/transport>
- [3] Transportation Research Board and National Academies of Sciences, Engineering, and Medicine, *An Update on Public Transportation’s Impacts on Greenhouse Gas Emissions*, The National Academies Press, Washington, DC, 2021. doi:10.17226/26103.
- [4] A. Nordelöf, M. Romare, J. Tivander, Life cycle assessment of city buses powered by electricity, hydrogenated vegetable oil or diesel, *Transportation Research Part D: Transport and Environment* 75 (2019) 211–222. doi:10.1016/j.trd.2019.08.019.
- [5] F. Héran, E. Ravalet, *La consommation d’espace-temps des divers modes de déplacement en milieu urbain: Application au cas de l’Ile de France*, Tech. rep., Ministère des transports, de l’équipement, du tourisme et de la mer (2008).
- [6] F. Cigarini, T.-A. Fay, N. Artemenko, D. Göhlich, Modeling and experimental investigation of thermal comfort and energy consumption in a battery electric bus, *World Electric Vehicle Journal* 12 (1) (2021). doi:10.3390/wevj12010007.
- [7] J. Brusey, D. Hintea, E. Gaura, N. Beloe, Reinforcement learning-based thermal comfort control for vehicle cabins, *Mechatronics* 50 (2018) 413–421. doi:10.1016/j.mechatronics.2017.04.010.
- [8] S. Schaut, O. Sawodny, Thermal management for the cabin of a battery electric vehicle considering passengers’ comfort, *IEEE Transactions on Control Systems Technology* 28 (4) (2020) 1476–1492. doi:10.1109/tcst.2019.2914888.
- [9] D. J. Docimo, A. G. Alleyne, Electro-thermal graph-based modeling for hierarchical control with application to an electric vehicle, in: 2018 IEEE Conference on Control Technology and Applications (CCTA), 2018, pp. 812–819. doi:10.1109/CCTA.2018.8511390.
- [10] J. Meyer, T. Kiss, L. Chaney, A new automotive air conditioning system simulation tool developed in MATLAB/Simulink, *SAE International Journal of Passenger Cars - Mechanical Systems* 6 (2) (2013) 826–840. doi:10.4271/2013-01-0850.

- [11] P. Bacher, H. Madsen, Identifying suitable models for the heat dynamics of buildings, *Energy and buildings* 43 (7) (2011) 1511–1522. doi:10.1016/j.enbuild.2011.02.005.
- [12] S. Privara, J. Cigler, Z. Vána, F. Oldewurtel, C. Sagerschnig, E. Žáčková, Building modeling as a crucial part for building predictive control, *Energy and Buildings* 56 (2013) 8–22. doi:10.1016/j.enbuild.2012.10.024.
- [13] F. Oldewurtel, A. Parisio, C. N. Jones, D. Gyalistras, M. Gwerder, V. Stauch, B. Lehmann, M. Morari, Use of model predictive control and weather forecasts for energy efficient building climate control, *Energy and buildings* 45 (2012) 15–27. doi:10.1016/j.enbuild.2011.09.022.
- [14] J. Drgoňa, J. Arroyo, I. C. Figueroa, D. Blum, K. Arendt, D. Kim, E. P. Ollé, J. Oravec, M. Wetter, D. L. Vrabie, et al., All you need to know about model predictive control for buildings, *Annual Reviews in Control* 50 (2020) 190–232. doi:10.1016/j.arcontrol.2020.09.001.
- [15] Y. Riachi, D. Clodic, A numerical model for simulating thermal comfort prediction in public transportation buses, *International Journal of Environmental Protection and Policy* 2 (1) (2014) 1–8. doi:10.11648/j.ijep.20140201.11.
- [16] M. Liebers, D. Tretsiak, S. Klement, B. Bäker, P. Wiemann, Using air walls for the reduction of open-door heat losses in buses, *SAE International Journal of Commercial Vehicles* 10 (2) (2017) 423–433. doi:10.4271/2017-01-9179.
- [17] H. Amri, R. N. Hofstädter, M. Kozek, Energy efficient design and simulation of a demand controlled heating and ventilation unit in a metro vehicle, in: 2011 IEEE Forum on Integrated and Sustainable Transportation Systems, 2011, pp. 7–12. doi:10.1109/FISTS.2011.5973605.
- [18] R. A. Haddad, H. Basma, C. Mansour, Modeling and control of heat pump system for battery electric buses, *Proceedings of the Institution of Mechanical Engineers, Part D: Journal of Automobile Engineering* 236 (14) (2022) 3201–3220. doi:10.1177/09544070211069465.
- [19] R. N. Hofstädter, J. Amaya, M. Kozek, Energy optimal control of thermal comfort in trams, *Applied Thermal Engineering* 143 (2018) 812–821. doi:10.1016/j.applthermaleng.2018.07.084.
- [20] C. Dullinger, W. Struckl, M. Kozek, A general approach for mixed-integer predictive control of HVAC systems using MILP, *Applied Thermal Engineering* 128 (2018) 1646 – 1659. doi:10.1016/j.applthermaleng.2017.09.104.
- [21] M. Sommer, E. Sax, T. Rösch, Model predictive hvac control with disturbance variable forecasting for city buses, in: 2021 International Conference on Electrical, Computer, Communications and Mechatronics Engineering (ICECCME), 2021, pp. 1–7. doi:10.1109/ICECCME52200.2021.9591111.
- [22] B. Beusen, B. Degraeuwe, P. Debeuf, Energy savings in light rail through the optimization of heating and ventilation, *Transportation Research Part D: Transport and Environment* 23 (2013) 50–54. doi:10.1016/j.trd.2013.03.005.
- [23] I. Cvok, I. Ratković, J. Deur, Multi-objective optimisation-based design of an electric vehicle cabin heating control system for improved thermal comfort and driving range, *Energies* 14 (4) (2021). doi:10.3390/en14041203.
- [24] C. Dullinger, W. Struckl, M. Kozek, A modular thermal simulation tool for computing energy consumption of HVAC units in rail vehicles, *Applied Thermal Engineering* 78 (2015) 616 – 629. doi:10.1016/j.applthermaleng.2014.11.065.
- [25] J. Vepsäläinen, K. Otto, A. Lajunen, K. Tammi, Computationally efficient model for energy demand prediction of electric city bus in varying operating conditions, *Energy* 169 (2019) 433–443. doi:10.1016/j.energy.2018.12.064.
- [26] H. Basma, C. Mansour, M. Haddad, M. Nemer, P. Stabat, Comprehensive energy modeling methodology for battery electric buses, *Energy* 207 (2020) 118241. doi:10.1016/j.energy.2020.118241.
- [27] H. Wang, H. Bi, Y. Zhou, C. Li, Field measurements and numerical analysis of the energy consumption of urban rail vehicle air-conditioning systems, *Applied Thermal Engineering* 177 (2020) 115497. doi:10.1016/j.applthermaleng.2020.115497.
- [28] D. Göhlich, T.-A. Ly, A. Kunitz, D. Jefferies, Economic assessment of different air-conditioning and heating systems for electric city buses based on comprehensive energetic simulations, *World Electric Vehicle Journal* 7 (3) (2015) 398–406. doi:10.3390/wevj7030398.
- [29] A. Pathak, M. Binder, F. Chang, A. Ongel, M. Lienkamp, Analysis of the influence of air curtain on reducing the heat infiltration and costs in urban electric buses, *International Journal of Automotive Technology* 21 (1) (2020) 147–157. doi:10.1007/s12239-020-0015-x.
- [30] G. Barone, A. Buonomano, C. Forzano, A. Palombo, Enhancing trains envelope – heating, ventilation, and air conditioning systems: A new dynamic simulation approach for energy, economic, environmental impact and thermal comfort analyses, *Energy* 204 (2020) 117833. doi:10.1016/j.energy.2020.117833.
- [31] C. Mansour, W. Bou Nader, F. Breque, M. Haddad, M. Nemer, Assessing additional fuel consumption from cabin thermal comfort and auxiliary needs on the worldwide harmonized light vehicles test cycle, *Transportation Research Part D: Transport and Environment* 62 (2018) 139–151. doi:10.1016/j.trd.2018.02.012.
- [32] F. Widmer, A. Ritter, M. Achermann, F. Büeler, J. Bagajo, C. H. Onder, Highly efficient year-round energy and comfort optimization of HVAC systems in electric city buses, *IFAC-PapersOnLine* 56 (2) (2023) 10656–10663, 22nd IFAC World Congress. doi:10.1016/j.ifacol.2023.10.715.
- [33] P. Ákos Szilassy, D. Földes, Consumption estimation method for battery-electric buses using general line characteristics and temperature, *Energy* 261 (2022) 125080. doi:10.1016/j.energy.2022.125080.
- [34] Z. Wang, J. Xu, Y. Wang, L. Wang, R. Wang, Annual energy simulation for the air conditioning of Fuxing high speed trains, *Applied Thermal Engineering* 188 (2021) 116591. doi:10.1016/j.applthermaleng.2021.116591.
- [35] C. Luger, J. Kallinovsky, R. Rieberer, Identification of representative operating conditions of HVAC systems in passenger rail vehicles based on sampling virtual train trips, *Advanced Engineering Informatics* 30 (2) (2016) 157–167. doi:10.1016/j.aei.2016.02.006.
- [36] C. Li, H. Wang, H. Bi, The calculation method of energy consumption of air-conditioning system in subway vehicle based on representative operating points, *IOP Conference Series: Earth and Environmental Science* 455 (1) (2020) 012177. doi:10.1088/1755-1315/455/1/012177.
- [37] A. Foda, M. Mohamed, M. Bakr, Dynamic surrogate trip-level energy model for electric bus transit system optimization, *Transportation Research Record* 2677 (1) (2023) 513–528. doi:10.1177/03611981221100242.
- [38] International Organization for Standardization, Building components and building elements – thermal resistance and thermal transmittance – calculation methods, ISO 6946:2017 (2017).
- [39] F. Sidler, S. Ineichen, G. Zweifel, *Messung Energieverlust durch Türöffnungen bei Linien-Bussen*, Schlussbericht 098 (des ESöV 2050-Programms), Bundesamt für Verkehr BAV (2019). URL <https://www.aramis.admin.ch/Grunddaten/?ProjectID=43762>
- [40] F. P. Incropera, D. P. DeWitt, T. L. Bergmann, A. S. Lavine, *Fundamentals of Heat and Mass Transfer*, 6th Edition, John Wiley & Sons, Hoboken, NJ, 2007.
- [41] A. Schälín, *Gebäudeeingänge mit grossem Publikumsverkehr*, Tech. rep., AFC Air Flow Consulting, Weinbergstr. 72, 8006 Zürich (Apr. 1998).
- [42] F. Sidler, F. Gubser, *Leistungsmessung an Bussen mit Türluftschleiern*, Schlussbericht 159 (des ESöV 2050-Programms), Bundesamt für Verkehr BAV (2021). URL <https://www.aramis.admin.ch/Grunddaten/?ProjectID=53131>
- [43] M. Mikofski, *Solar position calculator*, MATLAB Central File Exchange (2024). URL <https://ch.mathworks.com/matlabcentral/fileexchange/58405-solar-position-calculator>
- [44] Stadt Zürich, *Bauten – Blockmodell, Bauminventar* (2023). URL <https://www.stadt-zuerich.ch/ted/de/index/geoz/plan-und-datenbezug/3d-stadtmodell.html>
- [45] Federal Office of Topography swisstopo, *swissALTI3D* (2024). URL <https://www.swisstopo.admin.ch/en/height-model-swissalti3d>
- [46] D. E. Merino, A. Dubray-Demol, D. Dumur, E. Godoy, Control-oriented model of a reversible heat pump for electric vehicles, in: 2012 IEEE International Electric Vehicle Conference, 2012, pp. 1–6. doi:10.1109/IEVC.2012.6183160.
- [47] M. Salazar, F. Méndez, PID control for a single-stage transcritical CO2 refrigeration cycle, *Applied Thermal Engineering* 67 (1) (2014) 429–438. doi:10.1016/j.applthermaleng.2014.03.052.

- [48] C. Rostiti, S. Stockar, M. Canova, A rule-based control for fuel-efficient automotive air conditioning systems, in: SAE 2015 World Congress & Exhibition, SAE International, 2015. doi:10.4271/2015-01-0366.
- [49] International Organization for Standardization, Ergonomics of the thermal environment: Analytical determination and interpretation of thermal comfort using calculation of the PMV and PPD indices and local thermal comfort criteria, ISO 7730:2005 (2005).
- [50] P. O. Fanger, Thermal Comfort: Analysis and Applications in Environmental Engineering, Danish Technical Press, Copenhagen, Denmark, 1970.
- [51] M. das Neves Almeida, A. A. de Paula Xavier, A. O. Michaloski, A review of thermal comfort applied in bus cabin environments, Applied Sciences 10 (23) (2020). doi:10.3390/app10238648.
- [52] G. Havenith, D. Fiala, K. Błazejczyk, M. Richards, P. Bröde, I. Holmér, H. Rintamaki, Y. Benschabat, G. Jendritzky, The UTCI-clothing model, International Journal of Biometeorology 56 (2012) 461–470. doi:10.1007/s00484-011-0451-4.
- [53] U. Gross, K. Spindler, E. Hahne, Shapefactor-equations for radiation heat transfer between plane rectangular surfaces of arbitrary position and size with parallel boundaries, Letters in Heat and Mass Transfer 8 (3) (1981) 219–227. doi:10.1016/0094-4548(81)90016-3.
- [54] F. Widmer, A. Ritter, C. H. Onder, ZTBus: A large dataset of time-resolved city bus driving missions, Scientific Data 10 (1) (2023) 687. doi:10.1038/s41597-023-02600-6.
- [55] J. A. E. Andersson, J. Gillis, G. Horn, J. B. Rawlings, M. Diehl, CasADi – A software framework for nonlinear optimization and optimal control, Mathematical Programming Computation 11 (1) (2019) 1–36. doi:10.1007/s12532-018-0139-4.
- [56] A. Wächter, L. Biegler, On the implementation of an interior-point filter line-search algorithm for large-scale nonlinear programming, Mathematical programming 106 (2006) 25–57. doi:10.1007/s10107-004-0559-y.
- [57] P. Amestoy, A. Buttari, I. Duff, A. Guermouche, J.-Y. L’Excellent, B. Uçar, MUMPS, in: Encyclopedia of Parallel Computing, Springer US, Boston, MA, 2011, pp. 1232–1238. doi:10.1007/978-0-387-09766-4_204.
- [58] E. Hambræus, M. Minotta Cuervo, Optimization of thermal comfort on electric buses: A comprehensive study on passenger satisfaction in Stockholm, Sweden, Ph.D. thesis, KTH Royal Institute of Technology (2023).
URL <https://urn.kb.se/resolve?urn=urn:nbn:se:kth:diva-334889>

h_{in}	Conv. heat transfer coeff. inside	8.01 $\frac{W}{m^2 K}$
h_{out}	Conv. heat transfer coeff. outside	20.67 $\frac{W}{m^2 K}$
h_{rh}	Conv. heat transfer coeff. at RH	2.1 $\frac{W}{m^2 K}$
k_s	Heat conduction coeff. through shell	6.86 $\frac{W}{m^2 K}$
l_{cab}	Cabin length	18.7 m
$N_{samples}$	Number of samples considered	7399
$P_{aircurt,0}$	Specified air curtain power usage	1020 W
\dot{Q}_{met}	Metabolic heat rate of one passenger	125.3 W
T_{depot}	Depot temperature (see (33))	K
$T_{rh,target}$	RH target temperature	70 °C
v_{cab}	Draft velocity inside the bus	0.1 $\frac{m}{s}$
V_{cab}	Cabin air volume	116.7 m ³
w_{cab}	Cabin width	2.6 m
$w_{door,tot}$	Combined width of the bus doors	4.42 m
α_{paint}	Solar absorptivity of the bus shell	30 %
γ	COP (see Figure 3)	–
γ_{ac}	COP in cooling mode (see Figure 3)	–
γ_{hp}	COP in heating mode (see Figure 3)	–
ϕ_{cab}	Relative humidity in the cabin	40 %
ρ_{air}	Air density	1.25 $\frac{kg}{m^3}$
σ	Stefan Boltzmann constant	$5.67 \cdot 10^{-8} \frac{W}{m^2 K^4}$
τ_{vcc}	Time const. of first order VCC dynamics	20 s
τ_{win}	Solar transmissivity of the windows	46 %
$\zeta_{aircurt}$	Door loss reduction by air curtains	60 %
ζ_{int}	Frac. of heat absorbed by interior	30 %
ζ_{roof}	Frac. of roof covered by components	66 %
ζ_{win}	Frac. of walls consisting of windows	35.4 %

A. Model Constants

A_i	Area of passenger surface i	m ²
A_{int}	Surface area of the interior	20 m ²
A_{rh}	RH surface area	4 m ²
A_{roof}	Roof area	48.6 m ²
A_s	Total cabin shell area	199.5 m ²
A_{wall}	Cabin wall area	102.2 m ²
C_{cab}	Heat capacity cabin air	146.6 $\frac{kJ}{K}$
C_d	Door model discharge coefficient	0.6
C_{int}	Heat capacity interior	78 $\frac{kJ}{K}$
$c_{p,air}$	Specific heat capacity of air	1005 $\frac{J}{kg K}$
C_{rh}	Heat capacity of RHs	4800 $\frac{kJ}{K}$
$C_{s,i}$	Heat capacity cabin shell inside	856.1 $\frac{kJ}{K}$
$C_{s,o}$	Heat capacity cabin shell outside	856.1 $\frac{kJ}{K}$
$f_{ann,T_{co}}$	ANN function predicting PMV (see (32))	–
$F_{int \rightarrow s,i}$	View factor interior to shell inside	94 %
$F_{rh \rightarrow int}$	View factor RH to interior	30 %
$F_{rh \rightarrow s,i}$	View factor RH to shell inside	70 %
g	Earth’s gravitational acceleration	9.81 $\frac{m}{s^2}$
h_{cab}	Cabin height	2.4 m
h_{door}	Height of the doors	1.95 m